Full-Wave and Ray-Based Modeling of Cross-Beam Energy Transfer Between Laser Beams with Distributed Phase Plates and Polarization Smoothing

Introduction

In direct-drive inertial confinement fusion (ICF), a millimeter-scale spherical capsule is uniformly illuminated by symmetrically oriented laser beams.[1,2] The capsules have an outer ablator layer and an inner fuel layer. The lasers ablate the outer layer of the capsule, which generates pressure to implode the fuel. The ICF program relies on radiation–hydrodynamics codes for designing capsules and tuning laser conditions to optimize the hydrodynamic efficiency of implosions.[3] An essential component of these codes is a model for coupling laser energy to the capsule ablator.[4,5]

Laser energy is coupled to the ICF capsule primarily through electron–ion collisional absorption of the laser beams propagating through a coronal plasma that forms around the irradiated capsule.[6] Because the wavelength and period of the lasers are typically much smaller than the hydrodynamic spatial and temporal scales, respectively, the eikonal approximation can be used to solve the steady-state electromagnetic-field equations along ray trajectories using the instantaneous plasma conditions.[7]

In addition to collisional absorption, nonlinear laser–plasma interaction (LPI) processes affect laser-energy deposition. The main nonlinear processes that are thought to be energetically important in ICF experiments are the three-wave processes: stimulated Raman scattering (SRS), stimulated Brillouin scattering (SBS), and two-plasmon decay (TPD).[6] Stimulated Brillouin scattering is the parametric coupling between two electromagnetic waves and an ion-acoustic wave (IAW). When the seed and pump electromagnetic waves in the three-wave SBS process correspond to distinct laser beams, it is referred to as cross-beam energy transfer (CBET).[8,9]

Ray-based laser-energy deposition models that have been adapted to include CBET predict that laser absorption is reduced by ~10% to 20% (Ref. 4) and that laser-energy deposition uniformity is significantly modified in typical direct-drive ICF experiments.[3,10] Hydrodynamic simulations that include CBET show significantly better agreement with measured scattered-light spectra and implosion trajectories, but ray-based CBET calculations must still be modified using *ad hoc* multipliers and field limiters to give quantitative agreement with experimental observations.[11,12] In addition to the eikonal approximation,[7] ray-based CBET models that are used in radiation–hydrodynamics codes assume steady-state linear convective gains, pairwise coupling between rays, and local plane-wave laser beams. Direct-drive ICF experiments also employ polarization smoothing to improve drive-beam uniformity by splitting each laser beam into two beams with orthogonal polarization and a small angular divergence.[13,14] This is accounted for in ray-based models by assuming random relative polarizations of interacting beams and spatially averaged incoherence between the two polarization components of each beam.[15] A more-complete model of CBET is required to test the validity of these approximations.

This article compares wave- and ray-based CBET calculations in the presence of laser beam speckle and polarization smoothing using the full-wave LPI code *LPSE*.[16] The wave-based calculations suggest that laser beam speckle and polarization smoothing can lead to significantly more CBET than is predicted by ray-based calculations. To account for speckle effects in the ray-based model, a modification is presented that gives excellent agreement with wave-based calculations. Full-scale wave-based calculations in hydrodynamic profiles based on direct-drive experiments on the OMEGA laser suggest that beam speckle has a small (<1%) effect on direct-drive laser absorption.

This article (1) puts the current work in the context of previous work on the beam speckle's effect on CBET; (2) describes the ray-based CBET model; (3) describes the equations solved by *LPSE*; (4) compares the ray- and wave-based CBET models for a variety of laser and hydrodynamic configurations using both linearly polarized beams and beams with polarization smoothing; and (5) summarizes the conclusions.

Relation to Other Work

The theory of the speckle statistics of laser beams generated by distributed phase plates was developed using the formalism of Gaussian random fields.[17–20] There has been considerable theoretical work on the impact of laser speckle on filamentation,[21,22] deflection,[23,24] SBS,[25–27] and CBET in the paraxial approximation relevant to indirect-drive ICF.[28] Most of the previous studies of laser beam speckle in the ICF context have focused on ponderomotive self-focusing and filamentation. A recent study looked at the interaction between ponderomotive self-focusing and CBET.[29] The present study focuses on the effect of laser speckle on CBET in the absence of filamentation because this is the situation most relevant to direct-drive ICF experiments, where the single-beam laser intensities are typically well below the filamentation threshold and multi-beam filamentation should not be important.[30] The simulations were performed using a full-wave solver that does not make the paraxial approximation and solves the vector wave equation in 3-D, which is essential for studying direct-drive ICF where polarization smoothing is used and beams cross at arbitrary angles.

Ray-based modeling of laser-energy deposition and CBET is now routine in radiation–hydrodynamic simulations of ICF experiments.[4,5] Ray-based CBET models typically inject the beams as plane waves with an intensity equal to the spatially averaged intensity of the speckled laser beams that are used in the experiments. A recent study used the ray-based paraxial complex geometric optics (PCGO) approach to calculate CBET between speckled beams and compared the results to a paraxial wave-based code.[31] The PCGO approach gives a pseudo-speckle pattern that produces a statistical intensity distribution similar to a real speckle pattern over a limited range of speckle intensities. We present a ray-based model for calculating CBET between speckled beams that gives improved agreement with wave-based calculations by using ray tracing to directly solve the electromagnetic-field equations within the eikonal approximation.[7] This produces a real speckle pattern that, in the absence of CBET, exactly matches the wave-based calculation in regions of space where the eikonal approximation is valid and shows excellent agreement with the wave-based CBET calculations up to gains $\gtrsim 5$.

We also present a study of CBET between polarization-smoothed beams. Ray-based models rely on the assumption of uncorrelated polarization and phase to calculate the interaction between laser beams that employ polarization smoothing,[15]

but the limits of this approximation have not been previously studied because most previous studies were based on wave-based codes that solve only the scalar wave equation for the electromagnetic fields.

Ray-Based CBET Modeling

Cross-beam energy transfer is calculated along ray trajectories by numerically integrating the steady-state homogeneous gain along ray trajectories using the local plasma conditions.[32] The differential change in the energy of ray i at the jth location along its path caused by an interaction with ray k at the lth location along its path is[9]

$$\frac{dW_{ij}}{ds} = -\frac{W_{ij}}{\alpha_{ij}} + W_{ij}\xi_{ij}^{kl}\left(\frac{W_{kl}}{\varepsilon_0}\frac{dS_{k0}}{dS_{kl}}\right), \tag{1}$$

where $W_{ij} = \sqrt{\varepsilon_0}\left(dS_{ij}/dS_{i0}\right)\left|E_{ij}\right|^2$ is the ray energy, E_{ij} is the enveloped electric-field amplitude, $\varepsilon_0 = 1 - n_e/n_c$ is the permittivity, n_e is the electron density, $n_c = m_e\omega_0^2/(4\pi e^2)$ is the critical density for light with frequency ω_0, m_e is the electron mass, e is the electron charge, dS_{i0}/dS_{ij} is the ratio of the initial to current cross-sectional area of ray i (proportional to the ray intensity),

$$\xi_{ij}^{kl} = 5.88 \times 10^{-2}\frac{\lambda_0}{T_e\left(1 + 3T_i/ZT_e\right)}\frac{n_e}{n_c}\frac{\omega_s}{\nu_{IAW}}P\left(\eta_{ij}^{kl}\right),$$

$$P(\eta) = \frac{\left(\nu_{IAW}/\omega_s\right)^2\eta}{\left(\eta^2 - 1\right)^{2s} + \left(\nu_{IAW}/\omega_s\right)^2\eta^2},$$

$$\eta_{ij}^{lk} = \frac{\omega_{kl} - \omega_{ij} - \left(\mathbf{k}_{kl} - \mathbf{k}_{ij}\right)\cdot\mathbf{u}}{\omega_s},$$

λ_0 is the laser wavelength in vacuum (in microns), ω_{ij} is frequency of the ith ray at the jth location along its path in the lab frame and $\mathbf{k}_{ij}$ is the corresponding wave vector, ω_s is the acoustic frequency, ν_{IAW} is the IAW energy-damping rate, T_e (T_i) is the electron (ion) temperature in keV, Z is the ionization state of the ions, and $\mathbf{u}$ is the plasma flow velocity. α_{ij} is the local laser absorption length, which for electron–ion collisional absorption is equal to the group velocity over the

energy-damping rate $\alpha_{ij} = c\sqrt{\varepsilon_0}\, n_c / \nu_{ei} n_e$ evaluated at the local plasma conditions.[6] The collisional damping rate is $\nu_{ei} = \sqrt{2\pi}\, e^4 Z^2 n_i \Lambda_{ei} / \left(3\sqrt{m_e}\, T_e^{3/2}\right)$, where Λ_{ei} is the Coulomb logarithm.[33] Additional corrections related to laser absorption[34] and the temporal derivative of the background density profile[35] are included in ray-based models used in radiation–hydrodynamics codes, but these corrections were not used in the calculations here.

Equation (1) can be solved in numerous ways that all essentially come down to defining a procedure for breaking rays up into discrete segments and a procedure for mapping the energy of nearby rays onto a given section of a ray's path. The discretized version of Eq. (1) is

$$W_{i,j+1} = W_{ij} \exp\left[s_{ij}\left(-\frac{1}{\alpha_{ij}} + \sum_{kl}\frac{\xi_{ij}^{kl}}{\varepsilon_0}\frac{dS_{k0}}{dS_{kl}}W_{kl}\right)\right], \quad (2)$$

where s_{ij} is the length of the jth section of ray i's path. Equation (2) is a nonlinear system of equations that can be solved using fixed-point iteration,[36] but written in its current form it converges slowly because information about upstream changes along a ray propagate only one path step per iteration. The rate of convergence can be improved significantly by noting that

$$W_{ij} = W_{i0} \prod_{k=1}^{j} \frac{W_{ik}}{W_{i,k-1}},$$

where W_{i0} is the incident energy of the ith ray. Defining $\tilde{W}_{ik} \equiv W_{ik}/W_{i,k-1}$, Eq. (2) can be written as a fixed-point iteration over the $\tilde{W}_{ij}$,

$$\tilde{W}_{i,j+1} = \exp\left[s_{ij}\left(-\frac{1}{\alpha_{ij}} + \sum_{kl}\frac{\xi_{ij}^{kl}}{\varepsilon_0}\frac{dS_{k0}}{dS_{kl}}W_{k0}\prod_{m=1}^{l}\tilde{W}_{km}\right)\right], \quad (3)$$

which propagates information along complete ray paths on each iteration and has a negligible increase in computational cost for a single iteration because the term in brackets can be stored in terms of the W_{kl} by taking the cumulative product along the ray paths after each iteration.

The ray trajectories of geometrical optics are determined by solving the coupled ordinary differential equations

$$\frac{d\mathbf{x}}{d\tau} = \mathbf{k},$$

$$\frac{d\mathbf{k}}{d\tau} = \frac{1}{2}\nabla\varepsilon_0(\mathbf{x}), \quad (4)$$

where the wave-vector magnitude is normalized to the vacuum value $\left(k = \sqrt{\varepsilon_0}\right)$. The solution to Eq. (4) is single valued at every point in $(\mathbf{x}, \mathbf{k})$ phase space, but it does not necessarily have a single-valued projection onto x space.[7] The divisions between regions of the phase space solution that have a single-valued projection onto x space occur at caustics, and when the solution is divided into distinct sections that individually have single-valued projections onto x space, the regions are referred to as "sheets." In ray-based CBET calculations, a ray from each sheet interacts with every other sheet at a given point in x space. Accordingly, the sum in Eq. (3) is restricted to rays on distinct sheets. The time-enveloped electric field is reconstructed from the eikonal solution by summing over sheets:

$$\mathbf{E}(\mathbf{x}) = \sum_{j\,\text{sheets}} \mathbf{E}_j(\mathbf{x}) e^{i\phi_j(\mathbf{x})},$$

where ϕ_j is the phase corresponding to the field amplitude E_j. Additional subtleties are involved with ray-based CBET calculations at caustics because the electromagnetic-field amplitude in the eikonal approximation is singular. This topic will be discussed in a future publication (none of the ray-based calculations presented in this article included caustics).

The ray-based CBET calculations presented in this article discretized the ray trajectories on a Cartesian grid. Figure 151.12 shows a representation of the ray indexing scheme for two interacting beams, where rays 1 and 2 correspond to one beam and rays 3 and 4 correspond to the other beam. As an example of the indexing for the interactions, the crossing of rays 2 and 4 in grid cell 3 corresponds to the ray energies $W_{ij} \rightarrow W_{22}$ and $W_{kl} \rightarrow W_{42}$ with the interaction coefficient $\xi_{ij}^{kl} \rightarrow \xi_{22}^{42}$. Note that this example uses the ray energies at the grid cell entrance to calculate the interaction, but the numerical scheme converges to the same result if the midpoint or endpoint is used instead. Discretization onto a grid has the advantage of simplicity when determining the ray interactions because this step is reduced to simply looking at the other rays crossing a given grid cell, which also makes this step straightforward for parallel computation. The disadvantage, relative to interpolation-based
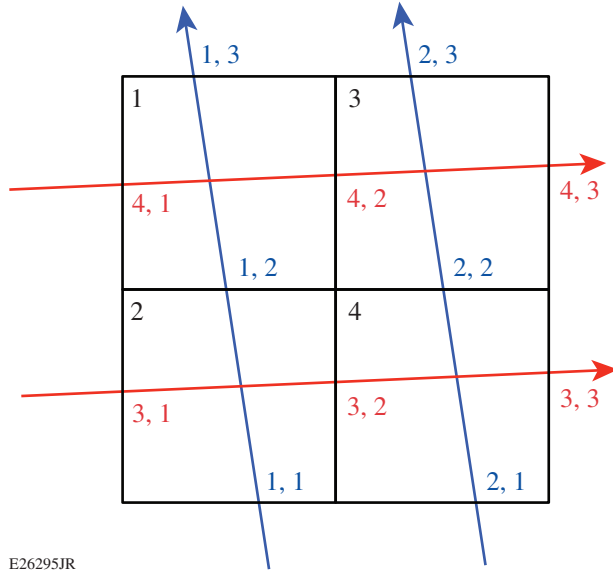
E26295JR

Figure 151.12
Indexing scheme for the ray paths and cross-beam energy transfer (CBET) grid for two interacting laser beams. The ray paths are divided according to their intersections with grid cell boundaries.

approaches, is that the rays must be dense enough that at least one ray from each sheet passes through each grid cell in the region where CBET is occurring for the solution to be valid.

1. **Speckle in Ray-Based CBET**

The laser beams used in ICF experiments pass through distributed phase plates (DPP's) that produce a speckle pattern consisting of many local minima and maxima at the focal plane.[13,19] The boundary condition for the electric field of a DPP beam injected at $z = 0$ can be modeled using

$$\mathbf{E}(x,y,z=0,t)=\sum_{\mathbf{k}}\left|\mathbf{E}(\mathbf{k},t)\right|e^{i(\mathbf{k}\cdot\mathbf{x}+\phi_{\mathbf{k}})}, \qquad (5)$$

where the sum is over beamlets generated by the DPP with distinct wave vectors $\mathbf{k}$ and random phases ($\phi_{\mathbf{k}}$) (Ref. 18). The eikonal solution for the electromagnetic fields with this boundary condition cannot be calculated from a single sheet of rays because the wavefront is not locally a plane wave, but it is a superposition of many plane waves, so the field is obtained by taking the coherent sum of the ray-trace solution for each term in Eq. (5). For a given boundary condition, this gives the same solution for the fields as the wave-based calculation in the absence of CBET (in regions of space where the eikonal approximation is valid). The superposition solution used to cal-

culate the fields cannot be applied to CBET, however, because the energy transfer is not linear in the electric field.[37]

To approximately include speckle effects in the ray-based CBET calculation, the local intensity variations were calculated using the superposition solution for the unperturbed electromagnetic fields and interpolated onto the ray trajectories used in the plane-wave calculation. The rest of the CBET calculation is identical to the plane-wave case with the intensity variations along the ray trajectories appearing as an additional term in the exponent in Eq. (3).

The primary increase in computational cost associated with the speckle model is that the speckles must be resolved on the CBET grid, which typically requires several-times-better spatial resolution for convergence than is needed for plane-wave beams. The transverse correlation length of a speckled beam is given by the product of the laser wavelength of the f number and the focusing optic ($f\lambda_0$) (Ref. 38), which is ~2 μm for the typical laser configurations used in ICF experiments (f/6.7 lenses and 0.351-μm light).[13]

We expect that a plane-wave approximation will be sufficient over some range of interaction configurations, and that the proposed model for including speckle effects in ray-based CBET calculations will extend this range, but a more-complete model is required to test the limits of these approximations.

LPSE

LPSE solves the time-enveloped Maxwell's equations coupled to the low-frequency plasma response in the fluid approximation. The plasma response is linearized around an inhomogeneous background density and flow velocity profile.[16] The time-enveloped wave equation for the electric field is

$$\frac{2i\omega_0}{c^2}\frac{\partial}{\partial t}\mathbf{E}+\nabla^2\mathbf{E}-\nabla(\nabla\cdot\mathbf{E})+\frac{\omega_0^2}{c^2}\varepsilon(\omega_0;\mathbf{x},t)\mathbf{E}=0,$$

where ε is the plasma dielectric function

$$\varepsilon(\omega_0;\mathbf{x},t)=1-\frac{\omega_{pe}^2(\mathbf{x},t)}{\omega_0(\omega_0+i\nu_{ei})}$$

and ν_{ei} is the electron–ion collision frequency. The physical electric field is given by $\tilde{\mathbf{E}}=\Re\left[\mathbf{E}(\mathbf{x},t)\exp(-i\omega_0 t)\right]$.

The equations for the low-frequency plasma response are

$$\left[\partial_t + \mathbf{U}_0(\mathbf{x}) \cdot \nabla \right]\left(\frac{\delta n}{n_0}\right) = -\mathcal{W},$$

$$\left[\partial_t + \mathbf{U}_0(\mathbf{x}) \cdot \nabla + 2\hat{v}_{\mathrm{IAW}}\right]\mathcal{W} = -\nabla^2\left[c_s^2\left(\frac{\delta n}{n_0}\right) + \frac{Ze^2}{4m_e m_i \omega_0^2}\left|\mathbf{E}\right|^2\right],$$

where $\mathcal{W} \equiv \nabla \cdot \delta\mathbf{U}$, $\mathbf{U}_0$ is the background flow profile, c_s is the sound speed, m_i is the ion mass, and $\hat{v}_{\mathrm{IAW}}$ is a phenomenological operator used to reproduce Landau damping of IAW's,[23] which is implemented by applying a constant damping of $v_{\mathrm{IAW}}/2$ in k space (the factor of 1/2 appears because v_{IAW} is the energy damping rate, and the damping is applied to the wave amplitudes in *LPSE*). The density is $n_e(\mathbf{x},t) = n_0(\mathbf{x}) + \delta n(\mathbf{x},t)$ and the flow velocity is $\mathbf{U}(\mathbf{x},t) = \mathbf{U}_0(\mathbf{x}) + \delta\mathbf{U}(\mathbf{x},t)$. *LPSE* uses a total-field/scattered-field approach, where the laser beams are injected inside of the total-field region and the scattered-field region acts as an absorbing boundary. Further details of the numerical algorithm and benchmarking can be found in Refs. 16 and 39.

Comparison Between *LPSE* Numerical Solutions and the Ray-Based Model

This section is divided into subsections corresponding to interactions between linearly polarized beams in a plasma with a constant density and linearly varying flow, interactions between linearly polarized beams in ICF-relevant plasma conditions, and interactions between beams with polarization smoothing.

1. Homogeneous Plasma

Figure 151.13 shows the magnitude of the steady-state electric field from a 2-D *LPSE* simulation of the interaction between two counter-propagating speckled beams in a plasma with a linear flow velocity profile given by $v_{\mathrm{flow}}(x) = -\hat{x}c_s(0.005x+1)$ and a constant density $n_e/n_c = 0.01$. The other plasma parameters were $T_e = 2$ keV, $T_i = 1$ keV, $Z = 3.1$, $A = 5.3$ (ion mass in amu), and $v_{\mathrm{IAW}}/\omega_s = 0.2$. The grid size was 80×240 μm^2 (3168×9504 grid cells) and the simulations were run until a steady state was established (4 ps). The speckle patterns correspond to $f/6.7$ lenses and were generated by launching 128 beamlets from each boundary with top-hat intensity distributions in wave-vector space [Eq. (5)] and fourth-order super-Gaussian distributions in physical space. The average initial intensity of the pump (seed) beam was 2×10^{15} W/cm^2 (1×10^{12} W/cm^2); both beams were polarized out of the plane (the average intensity is defined here as the peak intensity that
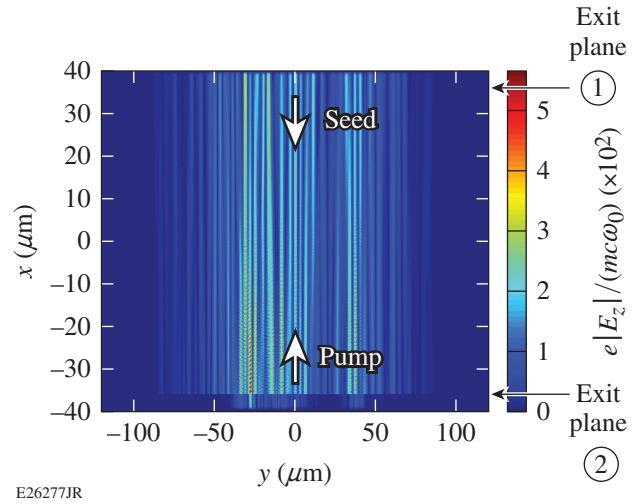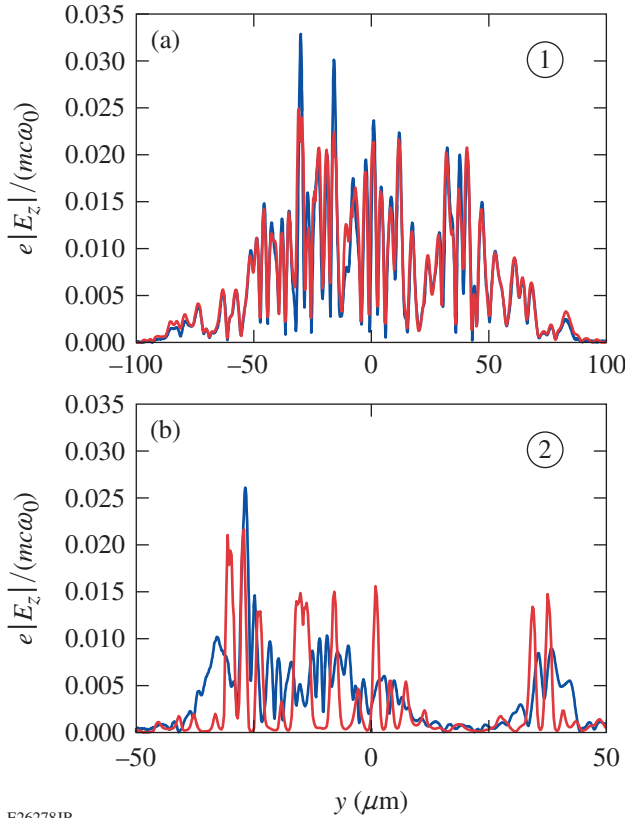

Figure 151.13
Magnitude of the time-enveloped electric field from an *LPSE* simulation of two counter-propagating beams with initial average intensities of 2×10^{15} W/cm^2 and 1×10^{12} W/cm^2.

a plane-wave beam would have for the same beam width and flux). The beams were launched 4 μm inside the simulation boundaries, and the outer 2 μm of the simulation grid were absorbing. The seed beam is not visible at its injection point ($x = 36$ μm) because of its low initial intensity, but it can be seen in the scattered region at the bottom of the image, where it exits with an average intensity of 3.2×10^{14} W/cm^2 corresponding to a gain of 5.8 (the gain is defined as the log of the incident seed-beam energy over the outgoing seed-beam energy).

Figure 151.14 shows lineouts of the *LPSE* field magnitude from Fig. 151.13 for the (a) pump and (b) seed beams at their respective exit planes (blue) and the corresponding result from the ray-based calculation (red). The two methods give nearly identical results for the field of the pump beam because it lost only 32% of its initial energy. The seed beam was amplified by more than 300×, and the two speckle patterns look completely different. Despite the significant differences in the structure of the calculated fields, the gain predicted by the ray-based model was only 0.8% lower than the wave-based calculation (the gain from the ray-based calculation using plane-wave beams was 38% lower). The ray-based calculation does not reproduce the detailed structure of the fields because the local variations in the direction of the wavefront were neglected when the magnitude of the fields was interpolated onto the ray trajectories from the plane-wave calculation. The interpolation procedure gives the correct statistical variations in the laser intensity, which is why the average CBET from the wave-based calculation was reproduced, but after energy is transferred, it is forced to fol-

E26278JR

Figure 151.14

(a) Lineout of Fig. 151.13 at $x = 37$ μm (blue), which corresponds to the scattered field of the pump beam. The corresponding lineout from the ray-based calculation is shown in red. (b) Similar lineouts at $x = -37$ μm corresponding to the scattered field of the seed beam. Labels (1) and (2) correspond to the exit plane labels in Fig. 151.13.

low the ray trajectories whereas it follows the local wavefront in the wave-based calculation.

The advantage of the ray-based calculation is a significant reduction in computational cost. The *LPSE* calculation depicted in Fig. 151.13 took one hour on 792 CPU cores, while the corresponding ray-based calculation took only a few minutes on a desktop computer. For a given grid resolution, the computational cost of the *LPSE* calculation is proportional to the number of grid cells $O(N_G)$. The relevant computational requirement for the ray-based CBET calculation is the number of pairwise interactions between rays, which is $O(N_G N_B^2)$, where N_B is the number of laser beams. The grid resolution in *LPSE* is determined by the need to resolve the wavelength of light, while in the ray-based calculation, it is necessary to resolve spatial variations in the laser intensity and hydrodynamic conditions. Although the quadratic dependence on the number of laser beams causes the ray-based calculation to scale

poorly to many beam systems, the grid resolution requirement is typically lower by a factor of 10 to 100 per dimension.

Figure 151.15 shows the results of a number of calculations similar to the one depicted in Fig. 151.13, where the pump intensity and the angle between the pump and seed beam were varied. The gains from the speckled-beam calculations are compared to those obtained in calculations that were identical except the speckled beams were replaced with plane-wave beams. For the case of counter-propagating beams, there is a difference of more than two e foldings in the energy gain for the speckled beams relative to the plane-wave beams at the highest pump intensity. At lower intensities, the difference diminishes. When the angle between the beams is increased, the difference between the plane-wave and speckled cases is reduced, and for more than 30° between the beams, there is no significant difference. Figure 151.15(d) shows the beam geometry used for these comparisons, which was chosen so that the peak of the CBET resonance was always at Mach 1.
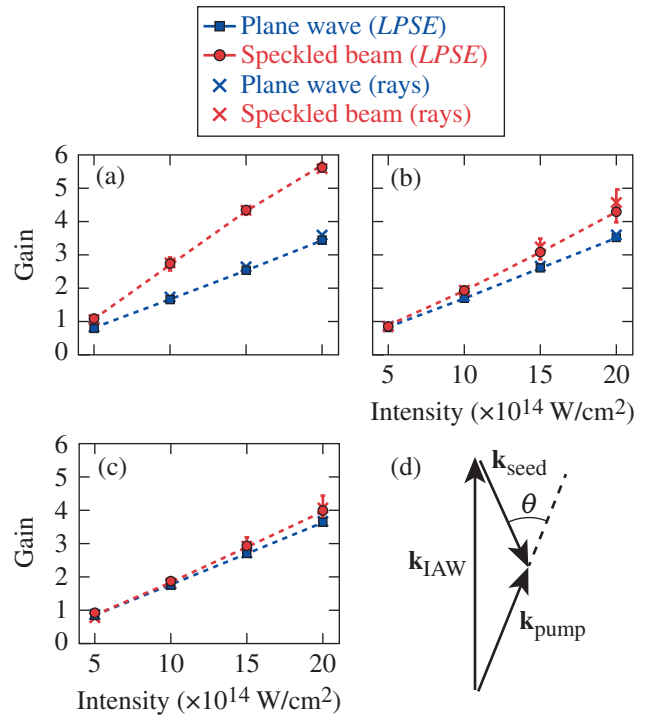
E26279JR

Figure 151.15

Gain as a function of laser intensity for beams separated by (a) 0°, (b) 15°, and (c) 30° relative to counter-propagating. The *LPSE* results are shown with red circles (speckled beams) and blue squares (plane-wave beams). The corresponding ray-trace results are shown with ×'s of the same color. The error bars correspond to the standard deviation in the gain over three different speckle realizations. (d) The beam geometry, where the wave vector of the resonant ion-acoustic wave (IAW) is antiparallel to the flow velocity gradient.

Figure 151.15 also shows the corresponding gains calculated using the ray-based CBET model. The ray-based model shows excellent agreement with the full-wave calculation for the interaction between plane waves, which indicates that the assumptions made in the ray-based model that are not related to beam speckle are valid in this configuration. The ray-based model also shows very good agreement with the speckled-beam results, and the calculated gains in the ray-based model always fall within one standard deviation of the *LPSE* gain averaged over different speckle realizations. The fact that the ray-based speckle model is in such good agreement with the wave-based calculations even when the plane-wave assumption gives a very poor approximation suggests that this is an extremely useful modification for including speckle effects in ray-based laser-plasma simulations. An additional benefit of the ray-based speckle model is that it inherently gives a more-realistic laser-energy deposition profile than a plane-wave approximation.

The maximum intensity used in Fig. 151.15 was chosen to keep the filamentation control parameter[38]

$$\left\langle \frac{P}{P_c} \right\rangle = 0.04 \, f^2 \left(\frac{n_e}{n_c} \right) \left(\frac{I_{14} \lambda_0^2}{T_e} \right) \tag{6}$$

below 1 (*f* is the *f* number and I_{14} is the laser intensity in units of 10^{14} W/cm^2). At the highest average intensity $\langle P/P_c \rangle = 0.22$. This is right at the limit where the highest-intensity speckles could potentially filament, but no filamentation was observed in the simulations depicted in Fig. 151.15. This was necessary for the comparison to the ray-based CBET model because the equations solved by *LPSE* implicitly include filamentation but the ray model does not.

The trends in Fig. 151.15 can be understood qualitatively by considering the average intensity over the CBET interaction region because the energy transfer is exponential in both the pump intensity and the interaction length. When the beams are counter-propagating, some of the speckles will see an increased pump intensity along the entire interaction length, giving exponentially larger gains, while the partially compensating reduction in the fraction of the beam profile that undergoes significant CBET is only a linear effect. When the angle between the beams is large, a given seed speckle will interact with many high- and low-intensity pump speckles, and the product of interaction length and pump intensity integrated over the interaction region averages out to the same value as for plane-wave beams. The same logic applies to the longitudinal extent of the speckles. In this example the speckles were longer

than the interaction region, but as the length of the interaction region is increased relative to the length of the speckles, the plane-wave gains are eventually recovered regardless of the relative beam orientation.

2. Amplitude of Density Perturbations

In addition to modifying the CBET gain, most of the CBET between speckled beams happens in localized hot spots, which can lead to larger density perturbations than occur when plane-wave beams interact. Figure 151.16 shows the ratio of root-mean-square (rms) density perturbations for a speckled-beam simulation and the corresponding plane-wave simulation. The ratio is always larger than 1, indicating that the typical density perturbation is larger for the speckled-beam interaction than for the plane-wave interaction. Although *LPSE* does not include the relevant physics, nonlinear effects become important at large $\delta n/n$ and cause CBET to saturate.[15,38] Note that the amplitude of the density perturbations is insensitive to the relative beam angle, which shows that this is not simply a result of increased CBET.
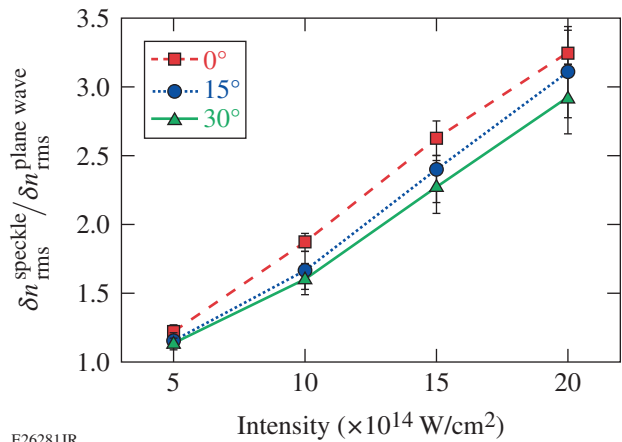

E26281JR

Figure 151.16
Root-mean-square (rms) density perturbation from *LPSE* simulations for the interaction between speckled beams divided by the rms density perturbation for the interaction between plane-wave beams. The rms perturbation was taken from the region $y = [-70,70]$ and $x = [0,30]$. The region was offset toward larger x so that the energy gain of the seed beam did not have a significant impact on the amplitude of the density perturbations. The error bars correspond to the standard deviation for three different speckle realizations.

To test the qualitative impact of nonlinear saturation, the *LPSE* simulations depicted in Fig. 151.15 were repeated with a clamp on the amplitude of the density perturbations $|\delta n/n| \leq 0.01$. This clamp was chosen to be more restrictive than the expected $|\delta n/n| \sim 0.1$ threshold[38] to exaggerate the impact of

nonlinear saturation. Previous studies using a code similar to *LPSE* have shown that an even more restrictive clamp on $\delta n/n$ is required to obtain quantitative agreement with scattered-light measurements in indirect-drive ICF experiments.[40] Figure 151.17 compares the *LPSE* gains plotted in Fig. 151.15 and the clamped simulations (only one speckle realization was simulated at each condition and compared to the corresponding simulation that used the same seed for random phase generation). At all relative beam angles and intensities, the perturbation-limited results are essentially indistinguishable for the plane-wave simulations, but in the speckled-beam simulations, the clamp reduced the amount of CBET significantly.

3. OMEGA Implosions

Although the subscale calculations presented in the previous section show that speckles can increase the CBET gain, the effect on laser absorption in direct-drive ICF experiments is expected to be small for two main reasons: (1) the single-beam intensities in ICF experiments are usually about an order of magnitude lower than the lowest intensity from Fig. 151.15; and (2) in a 3-D spherical implosion, the fraction of the solid angle that corresponds to nearly counter-propagating rays is small. The effect could be greater in indirect-drive ICF where many of the beams are nearly co-propagating although the single-beam intensities are still relatively low.[15]

Figure 151.18 shows the steady-state magnitude of the electric-field envelope and the corresponding ion-density perturbations for plane-wave and speckled-beam 2-D *LPSE* simulations of two *f*/6.7 *s*-polarized beams interacting in a realistic

direct-drive ICF plasma profile from the 1-D radiation–hydrodynamics code *LILAC*.[41] The beams were injected at normal incidence 22 μm inside the minimum *x* and *y* boundaries. The
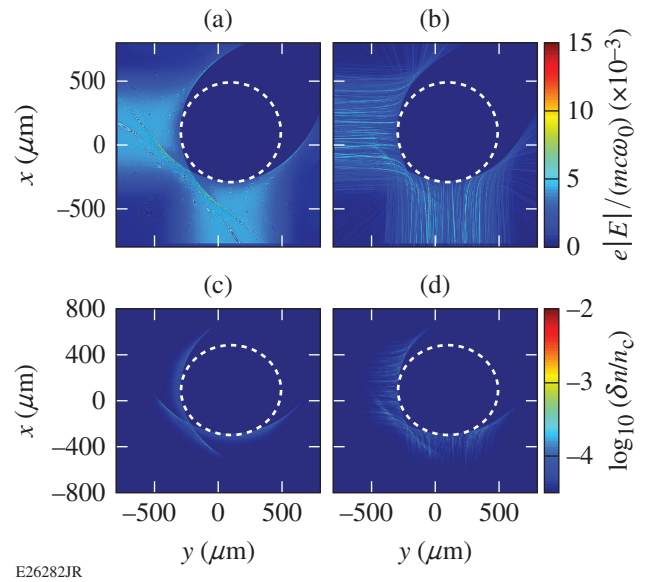

Figure 151.18
Amplitude of the electric-field envelope in a full-scale two-beam *LPSE* simulation (at 12 ps) using ICF-relevant plasma conditions with (a) plane-wave beams and (b) speckled beams at initial intensities of 2×10^{14} W/cm². The corresponding density perturbations are shown in (c) and (d). The critical density is denoted by white dashed circles. The electromagnetic-field (density-perturbation) grid was $40{,}000 \times 40{,}000$ ($80{,}000 \times 80{,}000$) cells. The small-scale rings in the fields are aliasing artifacts associated with the wavelength-scale perturbations on the high-resolution grids.
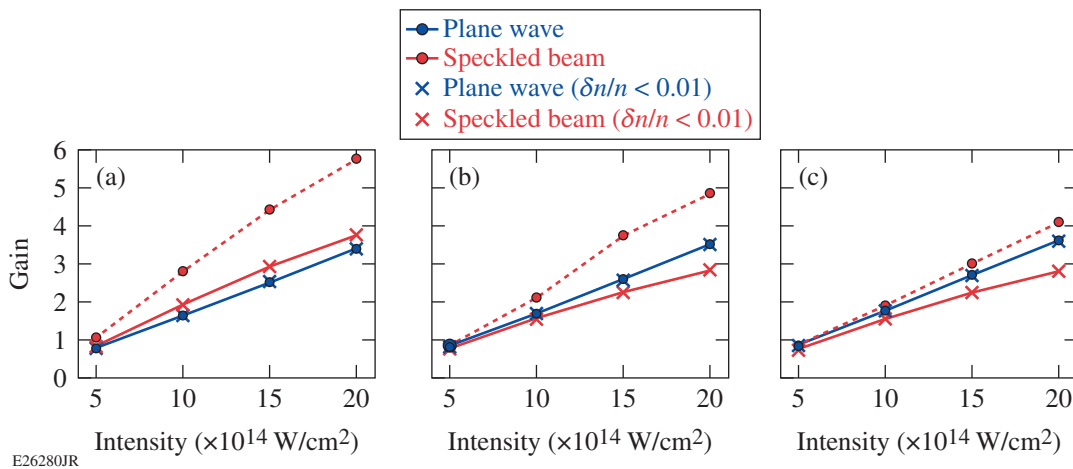

Figure 151.17
Gain as a function of pump intensity from *LPSE* simulations for speckled beams (red) and plane-wave beams (blue) with (circles) and without (crosses) a limiter of $|\delta n/n| \leq 0.01$ for beams separated by (a) 0°, (b) 15°, and (c) 30°.

angle between the beams was set to 90° because it gives nearly maximal CBET.[10] In Fig. 151.18(a), the field amplitude of the incident beams is visibly reduced after they cross through the caustic of the other beam. Because the outgoing portion of the beams gain energy from the incident beams, this interaction leads to a reduction in the total laser absorption. The density perturbations shown in Figs. 151.18(a) and 151.18(b) indicate where CBET occurs. The dominant interaction regions are in the beam caustics crossing through the middle of the other incoming beam and near to the critical density where the beams are reflected. The interaction at near-critical density is seeded by the reflected beam and is referred to as self-CBET. Self-CBET is typically not as energetically important as the interaction between distinct beams because it occurs at high densities and most of the energy that is transferred is still absorbed. The speckled-beam calculations are qualitatively similar to the plane-wave calculations in terms of where CBET occurs with the additional restriction that most of the CBET occurs in high-intensity speckles.

Two-beam simulations were performed at two different single-beam intensities, 1×10^{14} W/cm^2 and 2×10^{14} W/cm^2. These intensities are higher than the single-beam intensities in ICF experiments, but there are many more beams interacting in that case. The intensities were chosen to give a non-negligible reduction in laser absorption resulting from CBET while staying below the filamentation threshold. In the absence of CBET, the percentage of the incident laser energy that was absorbed by the plasma in the simulations similar to those shown in Fig. 151.18 was 94% regardless of beam type/intensity. For laser intensities of 1×10^{14} W/cm^2, the absorption was 90.5% (89.2%) for the plane-wave (speckled) beams, and for laser intensities of 2×10^{14} W/cm^2, the absorption was 85.4% (82.8%) for the plane-wave (speckled) beams. In both cases the reduction in laser absorption was ~30% larger for the speckled-beam simulations (relative to the no-CBET simulations). However, this configuration should significantly overestimate the impact of speckles because of the high single-beam intensities.

To test the effect of using many lower-intensity beams, 2-D quarter-scale, 16-beam *LPSE* simulations were run using single-beam intensities of 4×10^{14} W/cm^2. The beams were injected uniformly at 22.5° increments. In the quarter-scale, 16-beam configuration, the plane-wave simulation had 67% absorption and the speckled-beam simulation had 66.8% absorption (98% absorption without CBET). Despite the significant reduction in absorption caused by CBET, the plane-wave and speckled-beam simulations had nearly the same total laser absorption, which suggests that the use of many lower-intensity

beams smooths out single-beam speckle effects but does not diminish the impact of CBET.[30] Accordingly, a plane-wave approximation is expected to be sufficient for calculations of CBET between linearly polarized beams in many-beam direct-drive ICF applications.

4. Polarization Smoothing

Polarization smoothing is typically accounted for in ray-based CBET models by multiplying the gain coefficient calculated for parallel-polarized beams [ξ_{ij}^{kl} in Eq. (3)] by a factor of $(1 + \cos^2\theta)/4$, where θ is the angle between the interacting rays. This factor is obtained by assuming random relative polarizations of the interacting beams and spatially averaged incoherence between the two polarization components of each beam.[15] This approximation can be tested by comparing the ray model to *LPSE* simulations, which have full polarization effects.

Figure 151.19 shows the results of a series of comparisons between the *LPSE* and the ray-based model using polarization smoothing and two different *f* numbers (6.7 and 3) at pump-beam intensities of 5×10^{14} W/cm^2. The plasma conditions were the same as discussed in **Homogeneous Plasma** (p. 132) (homogeneous density and constant flow velocity gradient), and polarization smoothing was obtained by splitting the energy of the incident beams evenly between *s* and *p* polarizations. The two polarizations had statistically independent speckle realizations. The gain calculated by *LPSE* was higher than the gain in the ray-based model for all but the orthogonal *f*/3 beams. The gains are higher for the *f*/6.7 because their longitudinal correlation length ($2\pi f^2 \lambda_0 \approx 100$ μm) is longer than the interaction volume,[38] so the assumption of incoherence between the polarization components when averaged over the
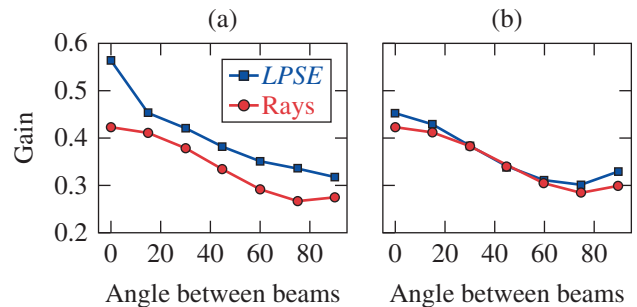
Figure 151.19

The CBET gain for a seed beam interacting with a pump beam at an intensity of 5×10^{14} W/cm^2. Both beams were smoothed by polarization with the energy split evenly between *s* and *p* polarization. The *f* numbers of the beams were (a) 6.7 and (b) 3. The wave-based (ray-based) results are shown in blue (red).

interaction region is violated. The speckle length for the $f/3$ beams is expected to be in better agreement with the ray-based calculation because of the reduced speckle length ($\sim 20~\mu$m).

There is a significant difference between the wave-based and ray-based results shown in Fig. 151.19, even though the intensity was only 5×10^{14} W/cm^2, and the gains were much lower than for the corresponding linearly polarized calculations. The discrepancy between *LPSE* and the ray-based model in the case where the beams are orthogonal is readily explained by noting that the in-plane components of the beams' polarizations do not interact, and the out-of-plane components have the same interaction as two linearly polarized beams with half of the energy. If the average intensity amplification for the linearly polarized case is written $I/I_0 = e^G$, then this should give $I/I_0 = \left(1 + e^{G/2}\right)/2$, whereas using the factor of $\left(1 + \cos^2\theta\right)/4$ gives $I/I_0 = e^{G/4}$.

In the case of counter-propagating beams, the difference can be understood by using a simple square-wave model, where a speckled beam is treated as having a beam spot profile with twice the average intensity over half of the beam profile and zero intensity over the rest. If the speckles are random, the interaction between two linearly polarized counter-propagating beams will have the same statistical properties as the interaction between the two beam profiles depicted in Fig. 151.20(a). The interaction can be broken up into four situations that occur with equal probability, only one of which results in any CBET (it is assumed here that the speckles are much longer than the interaction region). The expected intensity amplification is $\left(I/I_0\right)_{\text{speckle}} = \left(1 + e^{2G}\right)/2$. Comparing this to the amplification

using the average intensity $\left(I/I_0\right)_{\text{avg}} = e^G$, the first nonvanishing term in the Taylor expansion of the difference is $\left(I/I_0\right)_{\text{speckle}} - \left(I/I_0\right)_{\text{avg}} \approx G^2/2$, quadratic in the gain.

The same model can be used for polarization-smoothed beams, but each of the beams must also be split into two orthogonal polarizations. There are now four equally probable combinations of amplitude and polarization within each beam and 16 possible types of interactions between beams that are depicted in Fig. 151.20(b). Adding up the various contributions to the amplification gives $\left(I/I_0\right)_{\text{PS}} = 1/2 + \left(3e^G + e^{2G}\right)/8$. This should be compared to the amplification that is used in the ray-based model, $\left(I/I_0\right)_{\text{PS(rays)}} = e^{G/2}$, which to leading order gives $\left(I/I_0\right)_{\text{PS}} - \left(I/I_0\right)_{\text{PS(rays)}} \approx G/8$. The lowest-order correction is linear in G, consistent with the deviation between the wave- and ray-based calculations occurring at lower gains for polarization-smoothed beams than for linearly polarized beams.

The comparisons shown in Fig. 151.19 are useful for illustrating why CBET between polarization-smoothed beams might not agree with ray-based calculations, but they do not represent a fair comparison because the relative polarizations of the interacting beams were not random. Figure 151.21 shows the results of calculations where the initial polarization of the two beams was chosen randomly (and independently) before applying phase plates and polarization smoothing. For the $f/6.7$ beams, the average gain over realizations still differs from the ray-based model because of the large speckle length. The calculations using $f/3$ beams are in good agreement with the ray-based model, which suggests that the gain multiplier used to correct for polarization smoothing in the ray-based models is accurate when the underlying assumptions are satisfied.
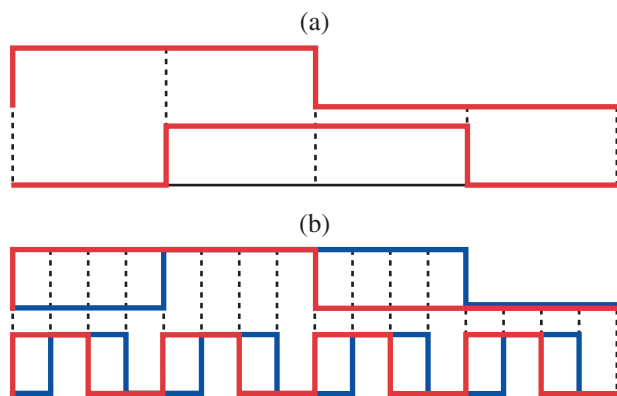

E26285JR

Figure 151.20
Beam profiles with the same statistical properties as a square-wave speckle model for (a) linearly polarized beams and (b) polarization-smoothed beams split evenly between s and p polarization.
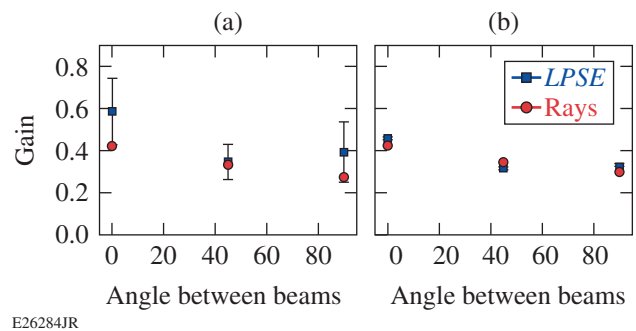

E26284JR

Figure 151.21
The average and standard deviations in the gain for different realizations of the relative beam polarization and various angles between the pump and seed beams (blue points with error bars). Twelve different realizations were used for (a) the $f/6.7$ beams and five realizations were used for (b) the $f/3$ beams. The red points show the corresponding results from ray-based calculations.

The discrepancy at larger *f* numbers could be significant in ICF experiments because the gradient scale lengths are typically comparable to the speckle length of the drive beams. In Fig. 151.18(c), the majority of the CBET is occurring in the "wings" in the lower left part of the image, where the caustic of the outgoing beam gains energy as it crosses the center of the incoming beam. The spatial extent of this transfer region is ≲100 μm.

Summary

The impact of beam speckle and polarization smoothing on CBET was studied using the full-wave LPI code *LPSE*. The results were compared to ray-based calculations using a code that is based on the ray models used to simulate ICF experiments. The ray-based model tends to underpredict the amount of CBET when the assumption of spatially averaged incoherence over the length of the interaction region is violated. A ray-based speckle model was presented that gives excellent agreement with the wave-based calculations over a broad range of gains and relative beam angles.

At all relative angles, the CBET interaction between speckled beams generates larger rms density perturbations than the corresponding plane-wave interaction. These enhanced density perturbations could lead to the earlier onset of nonlinear saturation of CBET between speckled beams. The single-beam intensities in ICF experiments are not sufficient for this effect to be significant, but it could play a role in many-beam interactions.

For linearly polarized beams, the large gain (≳1) and small relative beam angle that were required to see a significant difference between the plane-wave and speckled-beam calculations suggest that a plane-wave approximation should not result in a significant error in laser-absorption calculations for direct-drive ICF. This conclusion is supported by *LPSE* simulations in hydrodynamic profiles relevant to direct-drive ICF that showed a modest reduction in laser absorption for two-beam interactions and almost no reduction in laser absorption for a 16-beam interaction. For polarization-smoothed beams, there is a significant difference between the wave- and ray-based results at modest gains and over a broader range of relative beam angles, which could have an impact on CBET calculations for ICF.

REFERENCES

1. R. S. Craxton, K. S. Anderson, T. R. Boehly, V. N. Goncharov, D. R. Harding, J. P. Knauer, R. L. McCrory, P. W. McKenty, D. D. Meyerhofer, J. F. Myatt, A. J. Schmitt, J. D. Sethian, R. W. Short, S. Skupsky, W. Theobald, W. L. Kruer, K. Tanaka, R. Betti, T. J. B. Collins, J. A. Delettrez, S. X. Hu, J. A. Marozas, A. V. Maximov, D. T. Michel, P. B. Radha, S. P. Regan, T. C. Sangster, W. Seka, A. A. Solodov, J. M. Soures, C. Stoeckl, and J. D. Zuegel, Phys. Plasmas **22**, 110501 (2015).

2. S. Atzeni and J. Meyer-ter-Vehn, *The Physics of Inertial Fusion: Beam Plasma Interaction, Hydrodynamics, Hot Dense Matter*, International Series of Monographs on Physics (Clarendon Press, Oxford, 2004).

3. V. N. Goncharov, T. C. Sangster, R. Betti, T. R. Boehly, M. J. Bonino, T. J. B. Collins, R. S. Craxton, J. A. Delettrez, D. H. Edgell, R. Epstein, R. K. Follet, C. J. Forrest, D. H. Froula, V. Yu. Glebov, D. R. Harding, R. J. Henchen, S. X. Hu, I. V. Igumenshchev, R. Janezic, J. H. Kelly, T. J. Kessler, T. Z. Kosc, S. J. Loucks, J. A. Marozas, F. J. Marshall, A. V. Maximov, R. L. McCrory, P. W. McKenty, D. D. Meyerhofer, D. T. Michel, J. F. Myatt, R. Nora, P. B. Radha, S. P. Regan, W. Seka, W. T. Shmayda, R. W. Short, A. Shvydky, S. Skupsky, C. Stoeckl, B. Yaakobi, J. A. Frenje, M. Gatu-Johnson, R. D. Petrasso, and D. T. Casey, Phys. Plasmas **21**, 056315 (2014).

4. I. V. Igumenshchev, W. Seka, D. H. Edgell, D. T. Michel, D. H. Froula, V. N. Goncharov, R. S. Craxton, L. Divol, R. Epstein, R. Follett, J. H. Kelly, T. Z. Kosc, A. V. Maximov, R. L. McCrory, D. D. Meyerhofer, P. Michel, J. F. Myatt, T. C. Sangster, A. Shvydky, S. Skupsky, and C. Stoeckl, Phys. Plasmas **19**, 056314 (2012).

5. P. Michel *et al.*, Phys. Plasmas **17**, 056305 (2010).

6. W. L. Kruer, *The Physics of Laser Plasma Interactions*, Frontiers in Physics, Vol. 73, edited by D. Pines (Addison-Wesley, Redwood City, CA, 1988).

7. E. R. Tracy *et al.*, *Ray Tracing and Beyond: Phase Space Methods in Plasma Wave Theory* (Cambridge University Press, Cambridge, England, 2014).

8. R. W. Short and E. A. Williams, Phys. Rev. Lett. **47**, 337 (1981).

9. C. J. Randall, J. R. Albritton, and J. J. Thomson, Phys. Fluids **24**, 1474 (1981).

10. D. H. Edgell, R. K. Follett, I. V. Igumenshchev, J. F. Myatt, J. G. Shaw, and D. H. Froula, Phys. Plasmas **24**, 062706 (2017).

11. A. K. Davis, D. Cao, D. T. Michel, M. Hohenberger, D. H. Edgell, R. Epstein, V. N. Goncharov, S. X. Hu, I. V. Igumenshchev, J. A. Marozas, A. V. Maximov, J. F. Myatt, P. B. Radha, S. P. Regan, T. C. Sangster, and D. H. Froula, Phys. Plasmas **23**, 056306 (2016).

12. P. Michel *et al.*, Phys. Plasmas **20**, 056308 (2013).

13. T. R. Boehly, R. S. Craxton, T. H. Hinterman, J. H. Kelly, T. J. Kessler, S. A. Kumpan, S. A. Letzring, R. L. McCrory, S. F. B. Morse, W. Seka, S. Skupsky, J. M. Soures, and C. P. Verdon, Rev. Sci. Instrum. **66**, 508 (1995).

14. T. R. Boehly, V. A. Smalyuk, D. D. Meyerhofer, J. P. Knauer, D. K. Bradley, R. S. Craxton, M. J. Guardalben, S. Skupsky, and T. J. Kessler, J. Appl. Phys. **85**, 3444 (1999).

15. D. T. Michel, A. V. Maximov, R. W. Short, J. A. Delettrez, D. Edgell, S. X. Hu, I. V. Igumenshchev, J. F. Myatt, A. A. Solodov, C. Stoeckl, B. Yaakobi, and D. H. Froula, Phys. Plasmas **20**, 055703 (2013).

16. J. F. Myatt, R. K. Follett, J. G. Shaw, D. H. Edgell, D. H. Froula, I. V. Igumenshchev, and V. N. Goncharov, Phys. Plasmas **24**, 056308 (2017).

17. R. J. Adler, *The Geometry of Random Fields, Classics in Applied Mathematics* (Society for Industrial and Applied Mathematics, Philadelphia, 2010).

18. H. A. Rose and D. F. DuBois, Phys. Fluids B **5**, 590 (1993).

19. J. Garnier, Phys. Plasmas **6**, 1601 (1999).

20. J. Garnier and L. Videau, Phys. Plasmas **8**, 4914 (2001).

21. H. A. Rose and D. F. DuBois, Phys. Fluids B **5**, 3337 (1993).

22. A. J. Schmitt and B. B. Afeyan, Phys. Plasmas **5**, 503 (1998).

23. H. A. Rose, Phys. Plasmas **3**, 1709 (1996).

24. D. E. Hinkel *et al.*, Phys. Plasmas **6**, 571 (1999).

25. H. A. Rose, Phys. Plasmas **2**, 2216 (1995).

26. V. T. Tikhonchuk, C. Labaune, and H. A. Baldis, Phys. Plasmas **3**, 3777 (1996).

27. A. V. Maximov, J. Myatt, W. Seka, R. W. Short, and R. S. Craxton, Phys. Plasmas **11**, 2994 (2004).

28. P. Michel *et al.*, Phys. Plasmas **16**, 042702 (2009).

29. G. Raj and S. Hüller, Phys. Rev. Lett. **118**, 055002 (2017).

30. H. A. Rose and D. F. DuBois, Phys. Fluids B **4**, 252 (1992).

31. A. Colaïtis *et al.*, Phys. Plasmas **23**, 032118 (2016).

32. I. V. Igumenshchev, D. H. Edgell, V. N. Goncharov, J. A. Delettrez, A. V. Maximov, J. F. Myatt, W. Seka, A. Shvydky, S. Skupsky, and C. Stoeckl, Phys. Plasmas **17**, 122708 (2010).

33. J. D. Huba, NRL Plasma Formulary, Naval Research Laboratory, Washington, DC, Report NRL/PU/6790-94-265 (1994).

34. A. B. Langdon, Phys. Rev. Lett. **44**, 575 (1980).

35. T. Dewandre, J. R. Albritton, and E. A. Williams, Phys. Fluids **24**, 528 (1981).

36. L. R. Scott, *Numerical Analysis* (Princeton University Press, Princeton, NJ, 2011).

37. H. A. Rose and S. Ghosal, Phys. Plasmas **5**, 1461 (1998).

38. D. Pesme, S. Hüller, J. Myatt, C. Riconda, A. Maximov, V. T. Tikhonchuk, C. Labaune, J. Fuchs, S. Depierreux, and H. A. Baldis, Plasma Phys. Control. Fusion **44**, B53 (2002).

39. J. F. Myatt, J. G. Shaw, R. K. Follett, D. H. Edgell, D. H. Froula, I. V. Igumenshchev, and V. N. Goncharov, "*LPSE*—A 3-D Wave-Based Model of Cross-Beam Energy Transfer in Laser-Irradiated Plasmas," to be submitted to the Journal of Computational Physics.

40. P. Michel *et al.*, Phys. Rev. E **83**, 046409 (2011).

41. J. Delettrez, R. Epstein, M. C. Richardson, P. A. Jaanimagi, and B. L. Henke, Phys. Rev. A **36**, 3926 (1987).